CrossMark

Signatures of *r*-process Elements in Kilonova Spectra

Nanae Domoto[1] , Masaomi Tanaka[1] , Shinya Wanajo[2,3] , and Kyohei Kawaguchi[4,5]

[1] Astronomical Institute, Tohoku University, Aoba, Sendai 980-8578, Japan; n.domoto@astr.tohoku.ac.jp
[2] Max-Planck-Institut für Gravitationsphysik (Albert-Einstein-Institut), Am Mühlenberg 1, D-14476 Potsdam-Golm, Germany
[3] Interdisciplinary Theoretical and Mathematical Sciences Program (iTHEMS), RIKEN, Wako, Saitama 351-0198, Japan
[4] Institute for Cosmic Ray Research, The University of Tokyo, 5-1-5 Kashiwanoha, Kashiwa, Chiba 277-8582, Japan
[5] Center for Gravitational Physics, Yukawa Institute for Theoretical Physics, Kyoto University, Kyoto, 606-8502, Japan

Abstract

Binary neutron star (NS) mergers have been expected to synthesize *r*-process elements and emit radioactively powered radiation, called kilonovae. Although *r*-process nucleosynthesis was confirmed by the observations of GW170817/AT2017gfo, no trace of individual elements has been identified except for strontium. In this paper, we perform systematic calculations of line strength for bound–bound transitions and radiative transfer simulations in NS merger ejecta toward element identification in kilonova spectra. We find that Sr II triplet lines appear in the spectrum of a lanthanide-poor model, which is consistent with the absorption feature observed in GW170817/AT2017gfo. The synthetic spectrum also shows the strong Ca II triplet lines. This is natural because Ca and Sr are coproduced in the material with relatively high electron fraction and their ions have similar atomic structures with only one *s*-electron in the outermost shell. The line strength, however, highly depends on the abundance distribution and temperature in the ejecta. For our lanthanide-rich model, the spectra show the features of doubly ionized heavy elements, such as Ce, Tb, and Th. Our results suggest that the line-forming region of GW170817/AT2017gfo was lanthanide-poor. We show that the Sr II and Ca II lines can be used as a probe of physical conditions in NS merger ejecta. Absence of the Ca II line features in GW170817/AT2017gfo implies that the Ca/Sr ratio is <0.002 in mass fraction, which is consistent with nucleosynthesis for electron fraction $\geqslant 0.40$ and entropy per nucleon (in units of Boltzmann constant) $\geqslant 25$.

Unified Astronomy Thesaurus concepts: R-process (1324); Neutron stars (1108); Radiative transfer simulations (1967); Transient sources (1851)

1. Introduction

Coalescence of binary neutron stars (NSs) is a promising site for the rapid neutron capture nucleosynthesis (*r*-process; e.g., Lattimer & Schramm 1974; Eichler et al. 1989; Freiburghaus et al. 1999; Goriely et al. 2011; Wanajo et al. 2014). An NS merger ejects neutron-rich material, and heavy elements are synthesized in the ejecta. Then, radioactive decay of freshly synthesized nuclei powers electromagnetic emission, so-called kilonovae (Li & Paczyński 1998; Metzger et al. 2010; Roberts et al. 2011; Korobkin et al. 2012). A kilonova is expected to produce thermal emission mainly in ultraviolet (UV), optical, and near-infrared (NIR) wavelengths (Kasen et al. 2013; Barnes & Kasen 2013; Tanaka & Hotokezaka 2013).

NS mergers can generate several ejecta components reflecting the variety of mass ejection mechanisms. One is the dynamical ejecta component, which is promptly ejected after the merger with high velocity ($v \sim 0.2\,c$, where c is the speed of light) by tidal torque and shock heating (e.g., Rosswog et al. 1999; Hotokezaka et al. 2013; Sekiguchi et al. 2015). Another is the post-merger ejecta component from a subsequently formed accretion disk, which is driven by viscosity heating (e.g., Fernández & Metzger 2013; Just et al. 2015; Fujibayashi et al. 2018, 2020a). Mass ejection can be also enhanced by neutrino heating if the massive NS remnant survives (e.g., Ruffert et al. 1997; Perego et al. 2014; Fujibayashi et al. 2020c).

NS mergers are also the primary targets of gravitational wave (GW) observations. In fact, the first GW detection from an NS merger was successfully made in 2017 (GW170817, Abbott et al. 2017b). Through the intensive follow-up observations, an associated electromagnetic counterpart, AT2017gfo, was also identified (Abbott et al. 2017a). Observed properties of AT2017gfo in the UV, optical, and NIR wavelengths are broadly consistent with the theoretical expectation of kilonovae (e.g., Arcavi et al. 2017; Coulter et al. 2017; Evans et al. 2017; Pian et al. 2017; Smartt et al. 2017; Utsumi et al. 2017; Valenti et al. 2017).

It is important to figure out the abundance patterns that NS mergers produce. This leads toward understanding of not only the origin of heavy elements but also the physical conditions for NS merger ejecta, i.e., their masses, velocities, and electron fractions (the number of protons per nucleon, Y_e). When the ejecta have low Y_e ($\lesssim 0.25$), a strong *r*-process takes place and heavy elements including lanthanides ($Z = 57\text{--}71$) can be synthesized. Since lanthanides have high opacity in the ejecta, a kilonova is expected to show a long-lasting emission in the NIR wavelength ("red" component; Kasen et al. 2013; Tanaka & Hotokezaka 2013). On the other hand, if Y_e in the ejecta is relatively high ($Y_e \gtrsim 0.25$), the production of heavy elements is suppressed and lighter *r*-process elements can be synthesized (Metzger & Fernández 2014). Such ejecta can give rise to a short-time kilonova that is bright in the optical wavelength ("blue" component; Kasen et al. 2015; Tanaka et al. 2018). The time evolution of luminosity and color of AT2017gfo suggests the presence of both "red" and "blue" components (e.g., Kasen et al. 2017; Perego et al. 2017; Shibata et al. 2017; Tanaka et al. 2017; Kawaguchi et al. 2018; Rosswog et al. 2018). This has provided us with the evidence that NS mergers can certainly be the site of *r*-process nucleosynthesis.
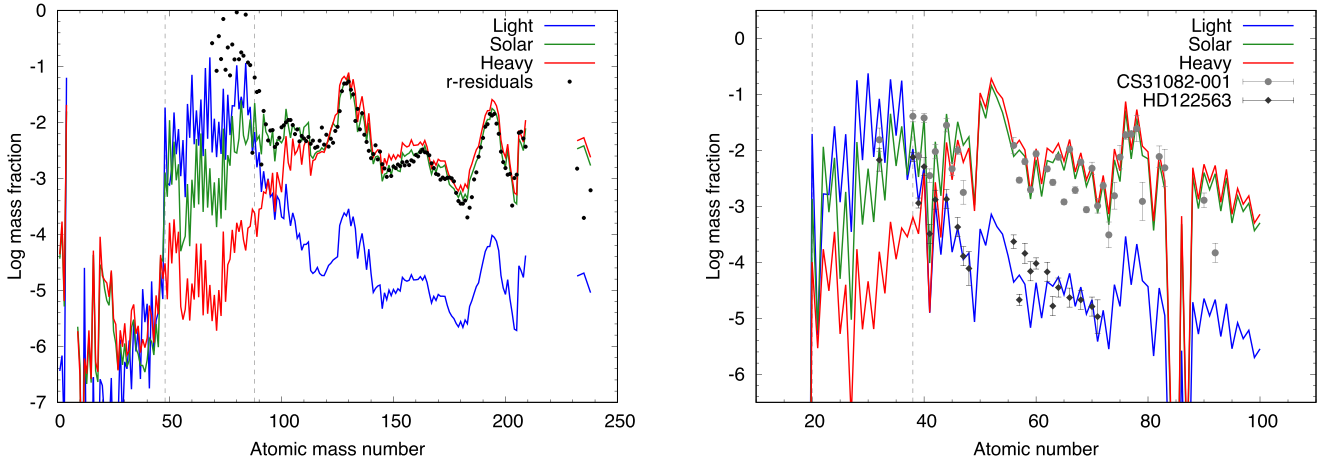
Figure 1. Left: final abundances for each model as a function of mass number. Black circles show the *r*-process residual pattern used for fitting (Prantzos et al. 2020). The residual abundances are scaled to match those for the S model at $A = 138$. Vertical dashed lines indicate ^{48}Ca and ^{88}Sr. Right: abundances for each model at $t = 1.5$ days as a function of atomic number. Abundances of an *r*-process-enhanced star CS 31082–001 (circles; Siqueira Mello et al. 2013) and an *r*-process-deficient star HD 122563 (diamonds; Honda et al. 2006; Ge from Cowan et al. 2005; Cd and Lu from Roederer et al. 2012) are also shown for comparison purposes. The abundances of CS 31082–001 and HD 122563 are scaled to those for the S and L models at $Z = 40$, respectively. Vertical dashed lines indicate Ca ($Z = 20$) and Sr ($Z = 38$).

It is not yet clear, however, which elements are synthesized in this NS merger. It is challenging to identify individual elements by using absorption features in the observed spectra since the absorption lines become broader and significantly overlapped in the high-velocity ejecta. In fact, no elements have been identified except for Sr in the spectra of GW170817/AT2017gfo (Watson et al. 2019). To extract elemental information from kilonova spectra, we need to understand which elements produce significant absorption lines in kilonova spectra by means of detailed theoretical calculations.

In this paper, we perform systematic calculations of line strength for bound–bound transitions and radiative transfer simulations in NS merger ejecta toward element identification in kilonova spectra. In Section 2, we show the line strength of elements for a simple one-zone model. Then, we perform radiative transfer simulations by assuming a one-dimensional ejecta structure in Section 3. We also discuss possible absorption features caused by other heavy elements in Section 4. Finally, we give our conclusions in Section 5.

2. Systematic Calculations of Line Strength

2.1. Methods

To investigate which elements produce strong absorption lines in the kilonova spectra, we systematically calculate the strength of bound–bound transitions for given density, temperature, and element abundances. The line strength is approximated by the Sobolev optical depth (Sobolev 1957) for each bound–bound transition,

$$\tau_l = \frac{\pi e^2}{m_e c} f_l n_{i,j} t \lambda_l \qquad (1)$$

for homologously expanding ejecta. The Sobolev approximation is valid for expanding matter with a large radial velocity gradient. Here $n_{i,j}$ is the number density of the lower level of the transition (*i*th ionized element in the *j*th excited state), and f_l and λ_l are the oscillator strength and the transition wavelength of the bound–bound transition, respectively. As in previous work on kilonovae (e.g., Barnes & Kasen 2013;

Tanaka & Hotokezaka 2013), we assume local thermodynamic equilibrium (LTE); we assume a Boltzmann distribution for the population of excited levels and solve the Saha equation to obtain ionization states.

Atomic data are essentially important to evaluate the line strength. For theoretical calculations of kilonova light curves, atomic data from theoretical calculations have often been used (e.g., Kasen et al. 2013; Tanaka et al. 2018; Banerjee et al. 2020; Fontes et al. 2020). This is useful in terms of completeness of data because the opacity of the ejecta should be correctly evaluated for the light-curve calculations (see Appendix A). However, while such theoretical data may give a reasonable estimate for the total opacity, they are not accurate in transition wavelengths, and thus not suitable for element identification. In this work, since we focus on the imprints of elemental abundances in kilonova spectra, we construct the latest line list based on the Vienna Atomic Line Database (VALD; Piskunov et al. 1995; Kupka et al. 1999; Ryabchikova et al. 2015). This database is suitable to identify lines because the transition wavelengths are calibrated with experiments and semiempirical calculations. It should be, however, noted that the line list is not necessarily complete, in particular, in the NIR region, although kilonovae are brighter in the NIR at late times. The impact of the incompleteness is discussed in Section 4.3.

For the abundance in the ejected matter from an NS merger, we use a multicomponent free-expansion (mFE) model in Wanajo (2018). This model is constructed as an ensemble of the parameterized outflows with constant velocity, initial entropy, and initial Y_e, which fit the *r*-process residuals of the solar abundances (Prantzos et al. 2020). The ranges of velocity (in units of *c*), entropy (in units of Boltzmann constant per nucleon, k_B/nucleon), and Y_e are taken to be 0.05–0.30, 10–35, and 0.01–0.50 with intervals of 0.05, 5, and 0.01, respectively, as in Wanajo (2018). Here we consider three models (left panel of Figure 1): (1) a model that fits the *r*-process residuals for $A \geqslant 88$, where A is mass number, i.e., including those heavier than the first *r*-process peak isotopes ($A = 80$–84); (2) a model that fits those for $A \geqslant 69$ (including the first *r*-process peak isotopes) and 3% of those for $A \geqslant 100$; and (3) a model that fits those for $A \geqslant 88$ and 1% of those for $A < 110$. Hereafter we

Table 1
Mass Fractions of Selected Elements

Model	X(Ca)[a]	X(Sr)[b]	X(La+Ac)[c]
Light (L)	1.8×10^{-2}	6.6×10^{-3}	4.9×10^{-4}
	2.0×10^{-2}	1.1×10^{-2}	5.9×10^{-4}
Solar (S)	1.3×10^{-3}	2.2×10^{-3}	0.09
	1.4×10^{-3}	3.3×10^{-2}	0.10
Heavy (H)	8.6×10^{-5}	2.4×10^{-4}	0.13
	1.0×10^{-4}	6.4×10^{-4}	0.15

Notes. The top rows show the final abundances, and the bottom rows show those at $t = 1.5$ days for each model.
[a] Mass fraction of calcium ($Z = 20$).
[b] Mass fraction of strontium ($Z = 38$).
[c] Sum of mass fractions for lanthanides ($Z = 57$–71) and actinides ($Z = 89$–100).

refer to these as the Solar (S), Light (L), and Heavy (H) models, respectively. Note that the S model is the same as mFE-b in Wanajo (2018), but the r-process residuals have been updated to those in Prantzos et al. (2020). The L model exhibits a similar abundance pattern to that of a metal-poor star with weak r-process signature (e.g., HD 122563, Honda et al. 2006; right panel of Figure 1). The H model represents a putative case, e.g., with a contribution from only dynamical ejecta. Note that the minimum mass number $A = 88$ for the S and H models corresponds to the dominant isotope of Sr, the element that has been measured in all r-process-enhanced stars (e.g., Cowan et al. 2021). We also performed the same calculations with the minimum mass number replaced by $A = 85$ (excluding the first r-peak and lighter isotopes) and 90 and confirmed that our results are unaffected by this choice.

Although these models include the abundances with $Z = 1$–110, we use only those with $Z = 20$–100 in our calculations at $t = 1.5$ days as shown in the right panel of Figure 1. The heaviest elements with $Z \geqslant 101$ are excluded because their mass fractions are very small ($\sim 10^{-6}$ to 10^{-4}), and there are no atomic data for such heavy elements. The light elements with $Z \leqslant 19$ are also excluded because their mass fractions are also small, on order of 10^{-4}, and they do not affect our results (see also Perego et al. 2020, for the effects of lightest elements). We summarize the mass fractions of selected elements for our models in Table 1. The distributions of Y_e for these models are shown in Figure 2 (see also Appendix B for the distributions of velocity and entropy). As can be anticipated from the abundance patterns (Figure 1), the distributions for the L and H models are dominated by higher (>0.3) and lower (<0.3) values of Y_e than those for the S model.

2.2. Results

The strength of bound–bound transitions at $t = 1.5$ days is displayed in Figure 3. As typical values in the ejecta (see Section 3), we evaluate the Sobolev optical depth for the density of $\rho = 10^{-14}\,\mathrm{g\,cm^{-3}}$ and temperature of $T = 5000\,\mathrm{K}$ (top panels) and $7000\,\mathrm{K}$ (bottom panels).

We find that the Sr II triplet lines (red lines at 10000–11000 Å) are strong for the L model in the case of $T = 5000\,\mathrm{K}$. Other notable features are the Ca II triplet lines (blue lines around 8500 Å), which are stronger than the Sr II lines. Note that Ca and Sr abundances in this model are dominated by ^{48}Ca and ^{88}Sr (see the left panel of Figure 1). For
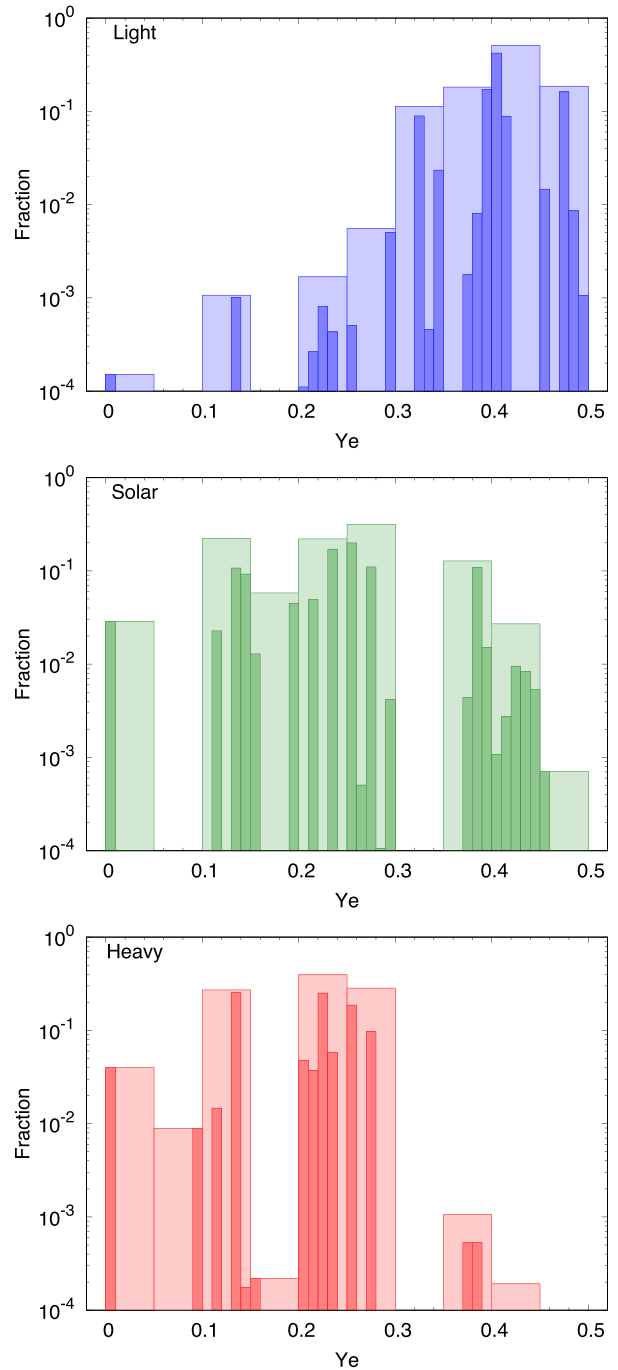

Figure 2. Histograms of electron fraction Y_e for the L (top), S (middle), and H (bottom) models. Denser colors show the histograms with an original interval ($\Delta Y_e = 0.01$), while lighter colors show those with a grouped interval ($\Delta Y_e = 0.05$).

higher temperature ($T = 7000\,\mathrm{K}$; bottom panel), these lines become significantly weaker.

In the S model, which has more heavy elements, either of the Sr II (red) or Ca II (blue) lines are not necessarily as strong as other lines of heavy elements, such as Tb III and Th III, when assuming $T = 5000\,\mathrm{K}$. For higher temperature ($T = 7000\,\mathrm{K}$), the Sr II and Ca II lines become significantly weaker as in the L model, while the strength of the Tb III and Th III lines is not largely affected. The results for the H model are similar to those for the S model.
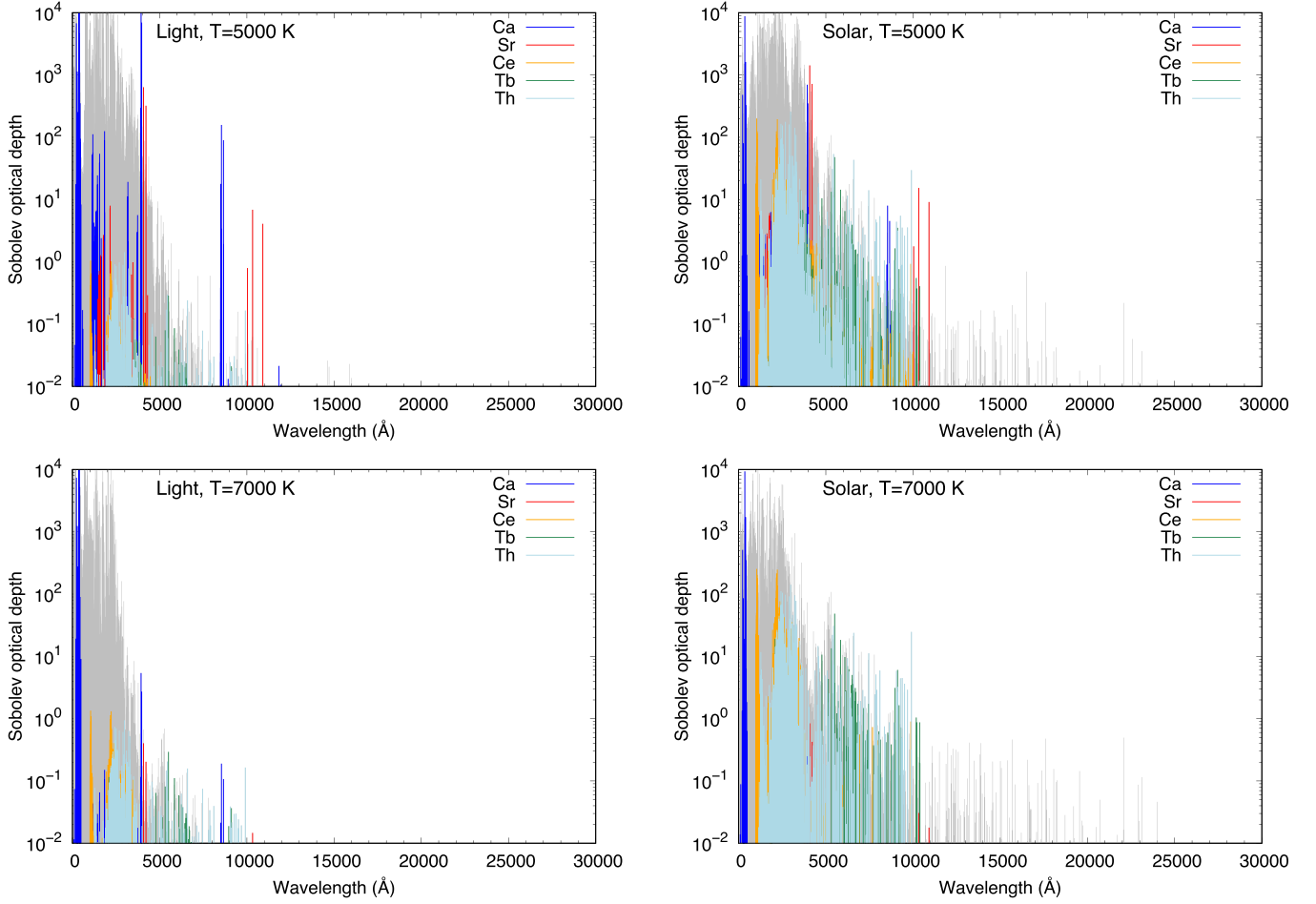
Figure 3. Sobolev optical depth of bound–bound transitions at $t = 1.5$ days. The elements with large contributions are shown with colors. The left panels show the results for the L model, while the right panels show those for the S model. The top and bottom panels correspond to two different temperatures, $T = 5000$ and 7000 K, respectively. For all the cases, the Sobolev optical depths are calculated with the density of $\rho = 10^{-14}$ g cm^{-3}.

The behavior of the line strength can be understood as the dependence of the Sobolev optical depths on temperature and density, as well as abundance distribution. Figure 4 shows the Sobolev optical depth for ranges of the density $\rho = 10^{-20}$ to 10^{-11} g cm^{-3} and temperature $T = 1000$–10,000 K. For the Ca II and Sr II lines, the strength of the middle line of each triplet (8452.088 Å for Ca II and 10327.31 Å for Sr II) is shown. Regarding Ce III lines, we choose one of the lines (9872.344 Å) as representative.

When we focus on the case with the density of $\rho = 10^{-14}$ g cm^{-3} as in Figure 3, the strength of the Ca II and Sr II lines is maximal around $T \sim 4000$ K. Then, the lines become weaker for higher temperature as these elements are ionized to the doubly ionized state. This is the reason why the models with $T = 5000$ K show the stronger Sr II and Ca II lines compared to those with $T = 7000$ K. On the other hand, the strength of the Ce III, Tb III, and Th III lines is maximal around $T \sim 6000$ K, and thus they do not show a large difference between $T = 5000$ and 7000 K. As a result, the line strength of these heavy elements becomes much more dominant than that of the Sr and Ca lines for $T = 7000$ K for the S and H models, in which these heavy elements are abundant.

It is natural that not only Sr II but also Ca II triplet lines become strong, because these elements have similar atomic structures. Figure 5 shows the energy levels and the transition wavelengths for these ions (NIST ASD; Kramida et al. 2019).

Both elements belong to group 2 in the periodic table and have only one electron in the outermost shell when they are singly ionized. The electron occupies the s shell in the ground state and has a relatively small number of excited levels. Therefore, the transition probability of each bound–bound transition tends to be high.

We confirm that the observed absorption feature around $\lambda \sim 8000$ Å in AT2017gfo is consistent with the Sr II triplet. Figure 6 shows the comparison between the spectrum of AT2017gfo at $t = 1.5$ days (Pian et al. 2017) and the result of the L model ($\rho = 10^{-14}$ g cm^{-3}, $T = 5000$ K). In this model, the wavelengths of the transitions are blueshifted owing to the adopted expansion velocity of $v = 0.2\,c$, which is suggested by the observations of AT2017gfo (e.g., Pian et al. 2017; Smartt et al. 2017). With this velocity, the wavelengths of the Sr II triplet (red) lines match the observed broad absorption feature, as also demonstrated by Watson et al. (2019). Note that Watson et al. (2019) included elements with $Z \geqslant 33$ in their calculations, i.e., Ca ($Z = 20$) was not included. Although our L model suggests that Ca II can also exhibit strong absorption lines, the spectrum of AT2017gfo does not show such a feature at $\lambda \sim 6800$ Å, an expected wavelength of the Ca II triplet with $v = 0.2\,c$. Implications of the absence of the Ca II lines in the observed spectrum are discussed in Section 4.2.
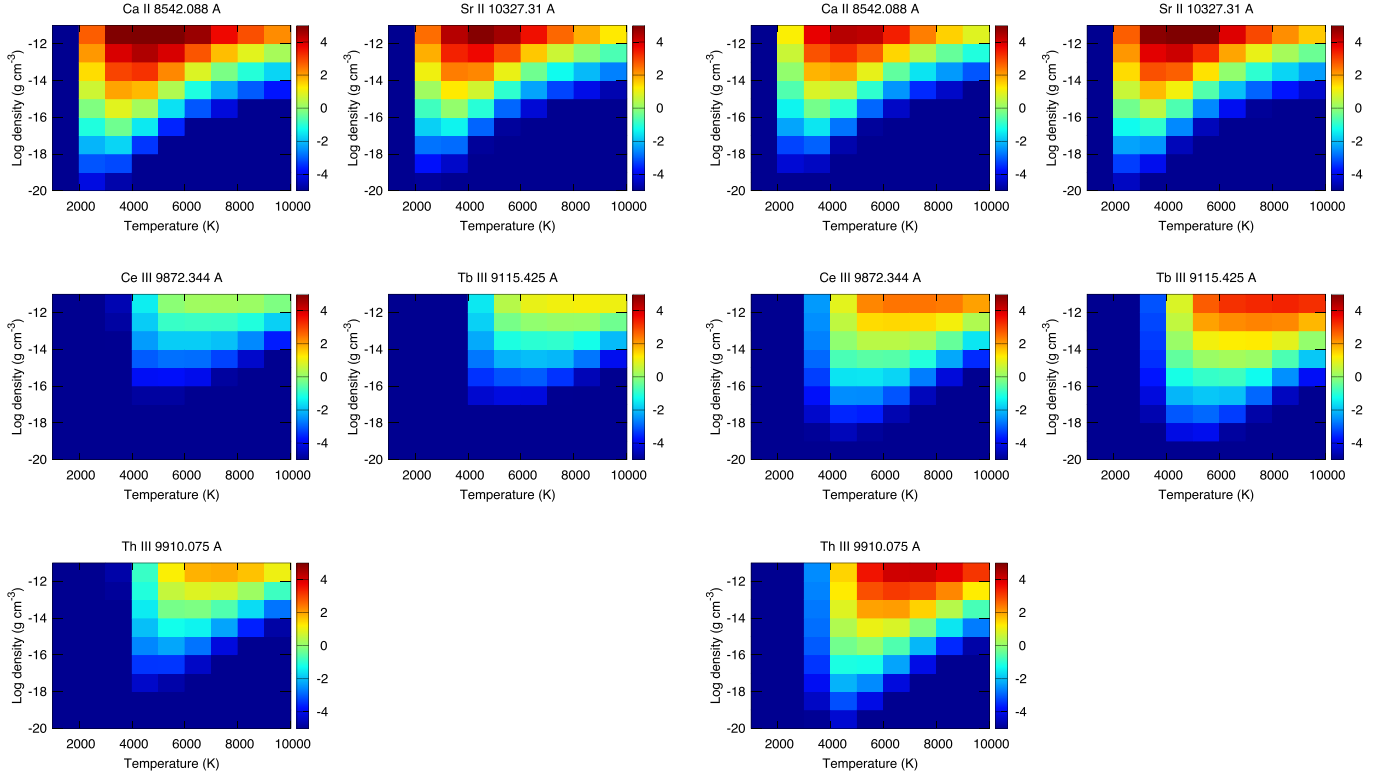
Figure 4. Density and temperature dependences of line strength at $t = 1.5$ days for representative transitions. Colors represent the Sobolev optical depth in logarithmic scale. The left five panels show the results for the abundance of the L model, while the right five panels show those of the S model. For both of the Ca II and Sr II triplet lines, we show the strength of the middle transitions.
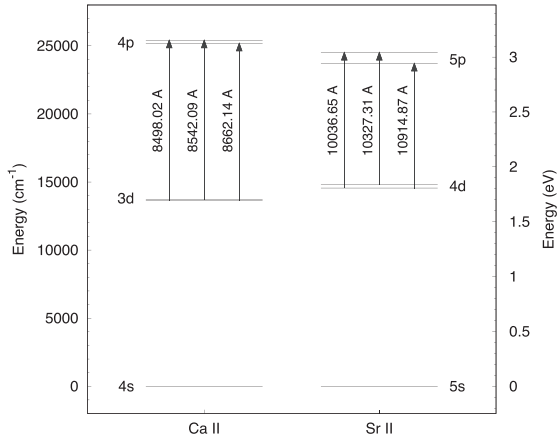

Figure 5. Energy diagrams for Ca II and Sr II. Each arrow shows the triplet transition with the value of the transition wavelength. The energy terms for these triplet lines are $^2D_{3/2}-^2P^o_{3/2}$, $^2D_{5/2}-^2P^o_{3/2}$, and $^2D_{3/2}-^2P^o_{1/2}$ from the shorter to longer wavelengths.

Figure 6. Comparison between the observed spectrum for AT2017gfo at $t = 1.5$ days (Pian et al. 2017) and the calculated Sobolev optical depth for the L model ($\rho = 10^{-14}$ g cm^{-3} and $T = 5000$ K). The positions of lines are blueshifted owing to the adopted expansion velocity of $v = 0.2\,c$. The gray shade shows the region of strong atmospheric absorption.

3. Synthetic Spectra

3.1. Methods

In this section, we calculate realistic synthetic spectra of kilonovae. The analysis in the previous section has evaluated the line strength for one-zone models. However, the ejecta from NS mergers have spatial distribution in density and temperature. Also, the temperature structure is controlled by radioactive heating and radiative transfer. Therefore, we perform radiative transfer simulations by taking the ejecta structure and radioactive heating into account. We use a wavelength-dependent radiative transfer simulation code (Tanaka &
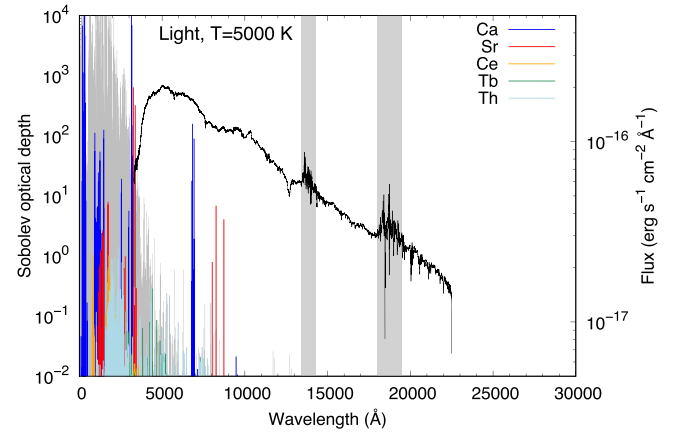
Hotokezaka 2013; Tanaka et al. 2014, 2017, 2018; Kawaguchi et al. 2018). The photon transfer is calculated by the Monte Carlo method. To compute the opacity for bound–bound transitions, we adopt the expansion opacity (Karp et al. 1977) and use the formula from Eastman & Pinto (1993):

$$\kappa_{\exp}(\lambda) = \frac{1}{ct\rho} \sum_l \frac{\lambda_l}{\Delta\lambda}(1 - e^{-\tau_l}), \qquad (2)$$

where τ_l is the Sobolev optical depth (Equation (1)). In the equation, the summation is taken over all the transitions within the wavelength bin $\Delta\lambda$. The Sobolev optical depths are
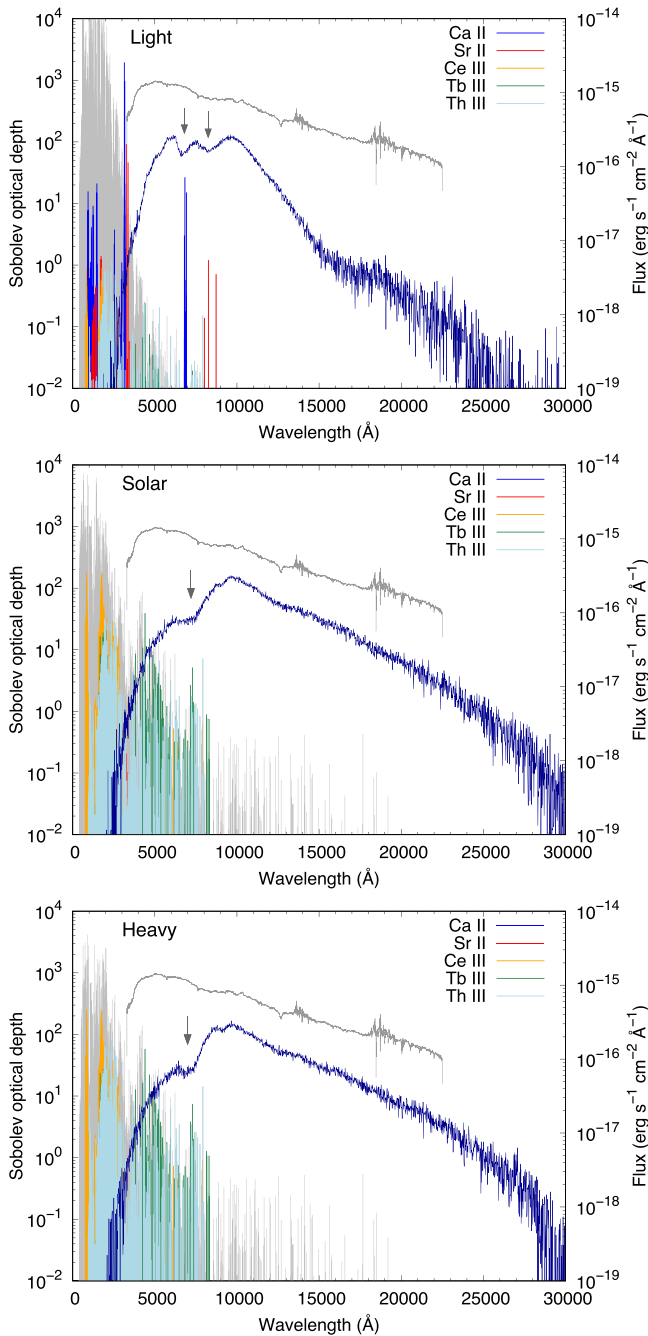
Figure 7. Synthetic spectra (blue curve) and line strength of each transition (vertical lines) at $t = 1.5$ days for the L (top), S (middle), and H (bottom) models. We plot the Sobolev optical depths in the ejecta at $v = 0.2\,c$. The positions of lines are blueshifted according to $v = 0.2\,c$. The gray curve in each panel shows the spectrum of AT2017gfo at $t = 1.5$ days, which is vertically shifted for comparison. Each arrow indicates the absorption lines that we focus on (see the text). The temperature in the ejecta at $v = 0.2\,c$ is $T \sim 5200$ K for the L model, while it is $T \sim 7200$ K for the S and H models.

evaluated in the same manner as in Section 2: we use the line list from the VALD database and assume LTE for ionization and excitation. Hereafter, we focus on the spectra at 1.5 days after the merger because insufficient atomic data in the NIR region start to affect the emission at later phases (see Section 4.3 and Appendix A).

For the ejecta density structure, we assume a single power law ($\rho \propto r^{-3}$) for the velocity range of the ejecta

$v = 0.05$–$0.3\,c$. The total ejecta mass is set to be $M_{\rm ej} = 0.03 M_\odot$. We use the three models for the abundance distributions as described in Section 2.1. The heating rate of radioactive nuclei is consistently taken from each model. The thermalization efficiency of γ-rays and radioactive particles follows the analytic formula by estimating characteristic timescales (Barnes et al. 2016).

3.2. Results

Figure 7 shows our results of synthetic spectra at $t = 1.5$ days after the merger. To show the contribution of different elements, we also plot the Sobolev optical depths in the ejecta at $v = 0.2\,c$. The wavelengths of lines are blueshifted according to $v = 0.2\,c$. This choice broadly captures the absorption features of the synthetic spectra, which indicates that the line-forming regions in the ejecta are formed around this velocity for our models.

The spectrum of AT2017gfo at $t = 1.5$ days (gray curve) is also plotted, which is vertically shifted for comparison. Our synthetic spectra do not necessarily reproduce the overall spectral shape: the L model underproduces the NIR flux, while the S and H models underproduce the optical flux. This is probably due to the assumption of the homogeneous abundance distribution in our models. It appears that a multicomponent model is needed to reasonably reproduce the observed spectrum of AT2017gfo (e.g., Kawaguchi et al. 2018). In this paper, therefore, we mainly focus on spectral features made by some elements.

We find that Sr II and Ca II produce absorption lines at $\lambda \sim 8000$ Å and $\lambda \sim 6500$ Å, respectively, in the spectrum of the L model (arrows in the top panel of Figure 7). This is reasonable since these triplet lines are stronger than other lines as shown in Section 2.2. The Sr II absorption feature at $\lambda \sim 8000$ Å is consistent with that seen in AT2017gfo, which is blueshifted according to $v = 0.2\,c$. This also supports the identification of this feature attributed to the Sr II lines (Watson et al. 2019).

For the S and H models, however, the Ca II and Sr II line features are overwhelmed by another broad absorption at around $\lambda \sim 7500$ Å (arrows in the middle and bottom panels of Figure 7), which is mainly caused by Ce III ($Z = 58$), Tb III ($Z = 65$), and Th III ($Z = 90$). The highest contribution comes from the Tb III and Th III lines (the rest-frame wavelength is 9115.425 Å for Tb III and 9910.075 Å for Th III), while the Ce III lines give a minor contribution. This is mainly due to the large fraction of heavy elements in the S and H models. Additional effects by the temperature are discussed in Section 4.1.

4. Discussion

4.1. Identification of Strontium and Other Heavy Elements

Our results confirm that the absorption feature at $\lambda \sim 8000$ Å in the spectrum of AT2017gfo can be caused by the Sr II triplet, as reported by Watson et al. (2019). However, it is emphasized that the Sr II lines are not always strongest: they give the strong absorption feature only in our lanthanide-poor (L) model but not in our lanthanide-rich (S or H) models. This suggests that the line-forming region of AT2017gfo at $t = 1.5$ days was lanthanide-poor (as discussed below).

Note that, in Watson et al. (2019), the absorption due to the Sr II triplet is strongest at $\lambda \sim 8000$ Å regardless of the
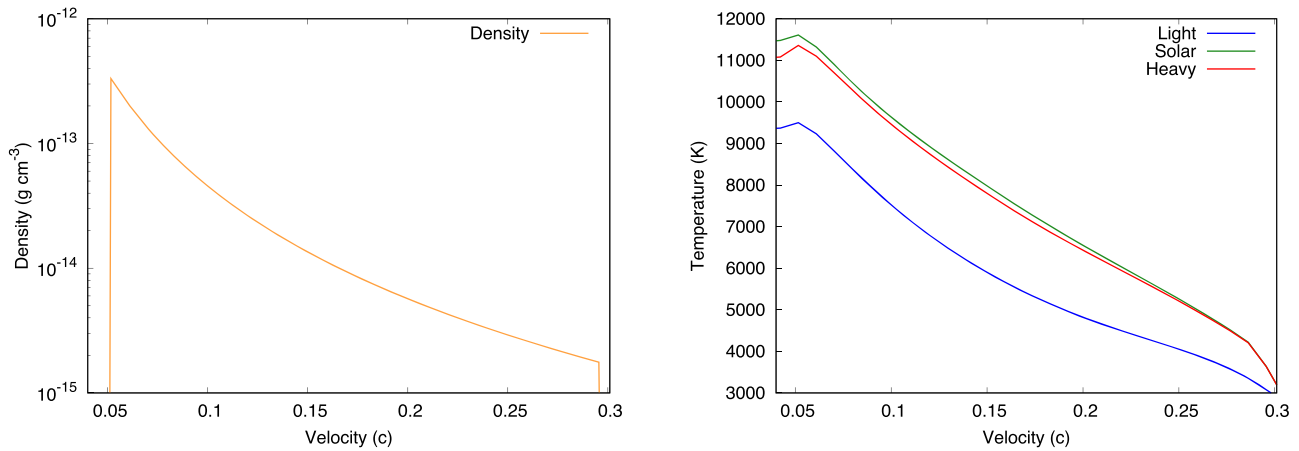
Figure 8. Density (left) and temperature (right) structures of the ejecta as a function of velocity at $t = 1.5$ days after the merger. The density structure is the same for the three models.

existence of heavy elements. As the strength of the Sr II lines is sensitive to the temperature (see Figure 4), this difference seems to be caused by the treatment of temperature in the ejecta. Our simulations take the structure of density and temperature in the ejecta into account and calculate the temperature from the radioactive heating rate in a consistent way. The temperature in the ejecta at $v = 0.2\,c$ is $T \sim 5200\,\mathrm{K}$ for the L model and $T > 7000\,\mathrm{K}$ for the S and H models. This difference is mainly caused by the higher heating rate for the latter models. Since these models synthesize heavier elements than those in the L model, the average radioactive heating rate is higher (Wanajo 2018). Also, when the ejecta have more heavy elements, the overall opacity becomes higher, which suppresses the radiative cooling (Kasen et al. 2013; Tanaka & Hotokezaka 2013; Tanaka et al. 2018). Therefore, in the S or H models, the temperature in the ejecta is higher than that in the L model for a fixed velocity.

To see the effect of abundance distribution and temperature on the line strength, we show the density and temperature structures in the ejecta in Figure 8 and the Sobolev optical depths for each model as a function of velocity in Figure 9. When we focus on the Sr II triplet lines, it is clear that they are strong in the L model. On the other hand, these lines are not necessarily strongest in the S and H models at the same velocity. Since the mass fraction of Sr is almost the same between the L and S models (see Table 1), the strength of Sr II lines is mainly affected by the temperature difference (see also Figure 4). Also, provided that the temperature is lower ($T \sim 5000\,\mathrm{K}$) in the S model, the Sr II line strength becomes comparable to those of heavy elements, as shown in Figure 3. Thus, the feature by the Sr II lines does not appear in the spectra of lanthanide-rich ejecta.

For the line strength of heavy elements, the abundance distribution plays a major role. As shown in Figure 3, the strength of Ce III, Tb III, and Th III lines is not largely changed between $T = 5000$ and $7000\,\mathrm{K}$, and they are comparable to or even stronger than other lines. Therefore, if the ejecta have a large amount of heavy elements as in the S model, the spectra show the feature of these heavy elements.

The optical depths in the S and H models are qualitatively similar, and thus the synthetic spectra of these models also become similar. The strength of Ca II and Sr II lines for the H model is weaker than that for the S model because of their smaller abundances (bottom panel of Figure 9). Note that a

significant difference between the spectra for the S and H models can appear at the later phase when the density and temperature in the ejecta decrease (see also Section 4.3).

Our results suggest that the absorption features depend on both temperature and abundance distribution in the ejecta. This means that different spectral features can appear in future kilonovae depending on, e.g., the ejecta masses and abundance distribution. In fact, our S and H models show spectra with absorption features by heavy elements such as Ce, Tb, and Th. The lines of these doubly ionized elements have been identified in chemically peculiar stars by using theoretical gf values (e.g., Ce III, Ryabchikova et al. 2006; Th III, Ryabchikova et al. 2007). Identification of such elements provides the direct evidence that heavy r-process elements are indeed synthesized in NS merger ejecta.

It should be noted that the transition probabilities of the doubly ionized ions of heavy elements are rather uncertain. The transition probabilities of these lines have been obtained only by theoretical calculations (Ce III, Biémont et al. 2002b; Th III, Biémont et al. 2002a; Tb III, Database on Rare Earths At Mons University, DREAM; Biémont et al. 1999), while those for singly ionized Ca and Sr are experimentally evaluated (e.g., Ca II, Theodosiou 1989; Sr II, Kurucz 2017). Since kilonova ejecta are expected to have a wide range of temperature and ionization states, more experimental and observational calibrations for transition probabilities are necessary (see also Section 4.3).

It is also cautioned that our models are calculated by assuming one-dimensional ejecta with homogeneous abundance distribution. It is not clear how multidimensional modeling will affect our results presented here, depending on the spatial distributions of, e.g., ejecta masses, velocities, and abundances. We leave such exploration to future work.

4.2. Strontium and Calcium as a Tracer of High-Y_e Ejecta

Our results suggest that the Sr II and Ca II triplet lines can be used as a tracer of high-Y_e ejecta. The L model shows a strong absorption feature of the Ca II lines, while the spectra of AT2017gfo do not exhibit such features. This implies that the abundance of Ca in the line-forming region of AT2017gfo is smaller than that in our L model. We perform the same radiative transfer simulations for the L model by varying the mass fraction of Ca to reconcile our model with the case for
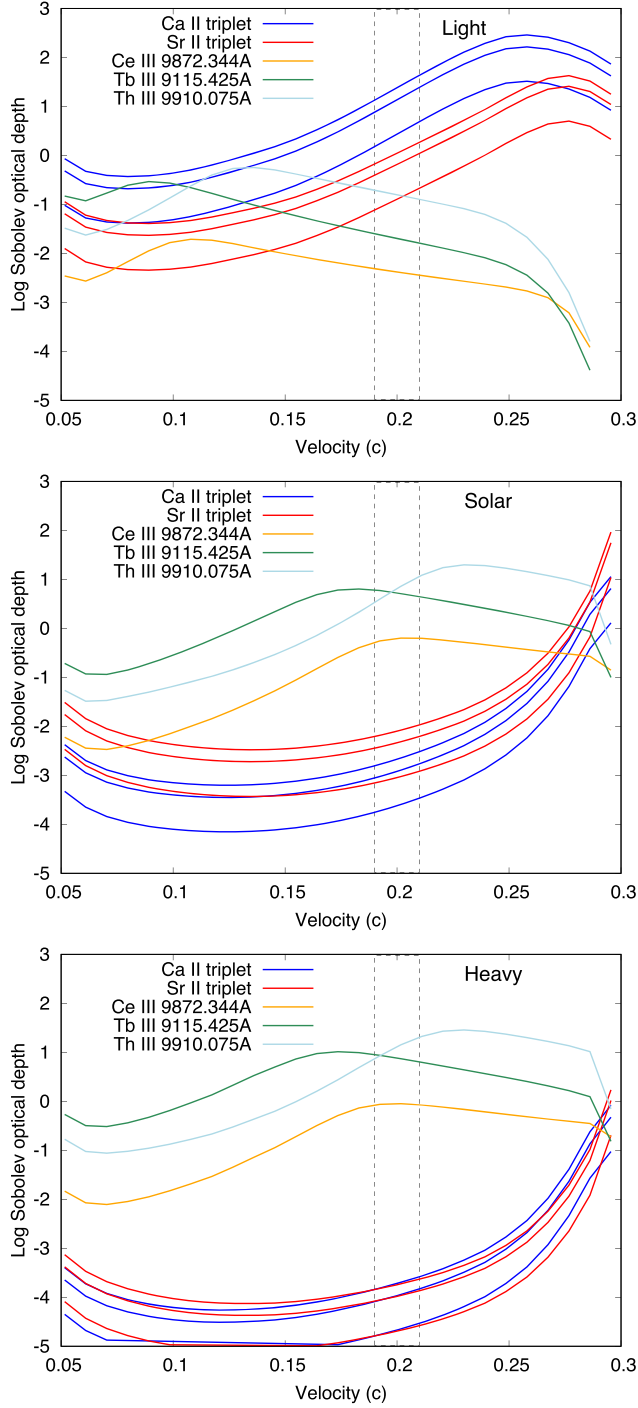
Figure 9. Distribution of the Sobolev optical depths as a function of velocity for the representative lines at $t = 1.5$ days after the merger. The top, middle, and bottom panels show the results for the L, S, and H models, respectively. The rectangle region (dashed line) in each panel indicates $v \sim 0.2\,c$.

Figure 10. Mass fractions of Ca (top) and Sr (middle) as a function of Y_e for the individual outflows with the various sets of velocity and entropy (gray lines). Colored lines show the results with $v = 0.2\,c$ and the six different entropies in the legend. The bottom panel shows the ratio of the mass fraction of Ca to that of Sr. The horizontal dashed line indicates $X(Ca)/X(Sr) = 0.002$, below which the absence of the Ca line in AT2017gfo can be explained. The Ca abundance is dominated by ^{48}Ca except for $Y_e \gtrsim 0.45$.

AT2017gfo. The result indicates that the Ca II lines disappear when the ratio $X(Ca)/X(Sr)$ is smaller than ~ 0.002.

To infer the relevant physical properties from this constraint, we show the mass fractions of Ca and Sr as a function of Y_e for the individual outflows (Section 2.1) with different velocities and entropies in Figure 10. We first focus on the range of $Y_e = 0.30$–0.50 as a relevant condition in the L model (Figure 2) and the velocity of only $v = 0.2\,c$, which is consistent with the blueshift of the Sr II triplet in AT2017gfo.
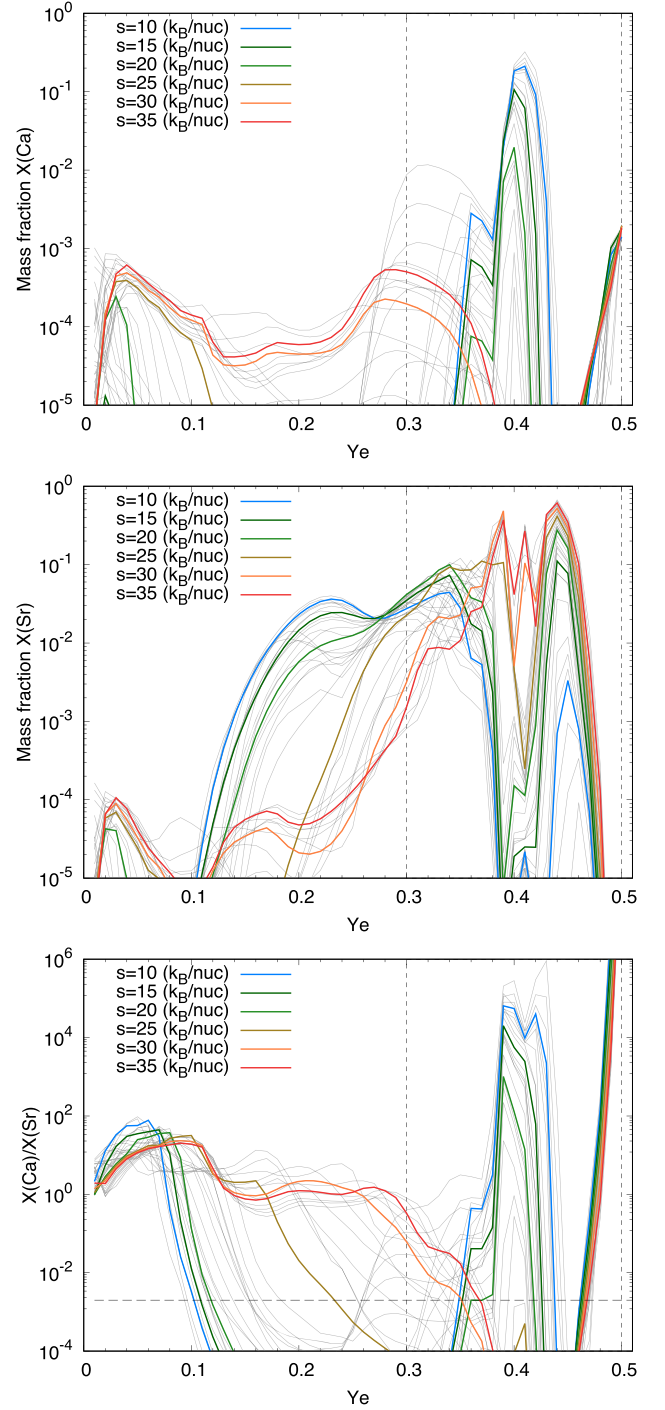
For these conditions, the Sr abundance (dominated by ^{88}Sr) is always relatively high (color lines in the middle panel), which is produced both in nuclear equilibrium and by neutron capture over a wide range of Y_e. By contrast, Ca, which is dominated by ^{48}Ca for $Y_e < 0.45$, is preferentially produced in nuclear equilibrium with Y_e near its proton-to-nucleon ratio of $20/48 = 0.417$ (Meyer et al. 1996; Wanajo et al. 2013). For this
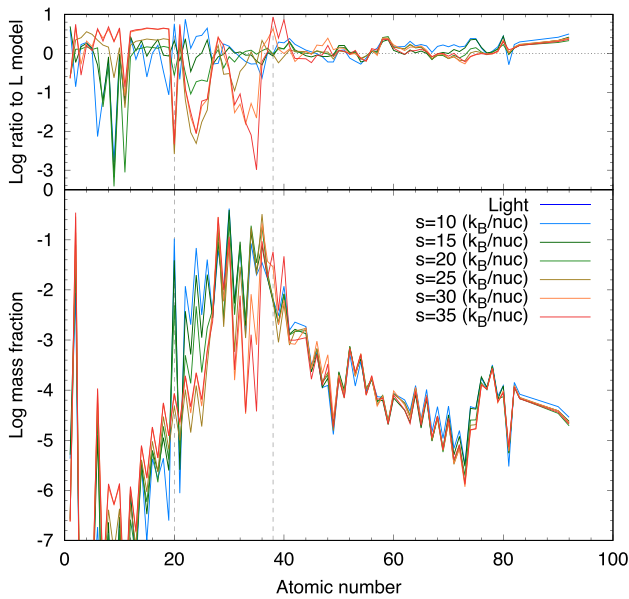
Figure 11. Final abundances for the individual outflows with the fixed velocity of $v = 0.2\,c$ and the six different entropies in the legend as a function of atomic number, compared to those for the L model. The top panel shows the ratio of abundances for each outflow to those for the L model. Dashed lines indicate Ca ($Z = 20$) and Sr ($Z = 38$). Abundances are not largely changed among these cases except for the range around $Z = 20$–40.
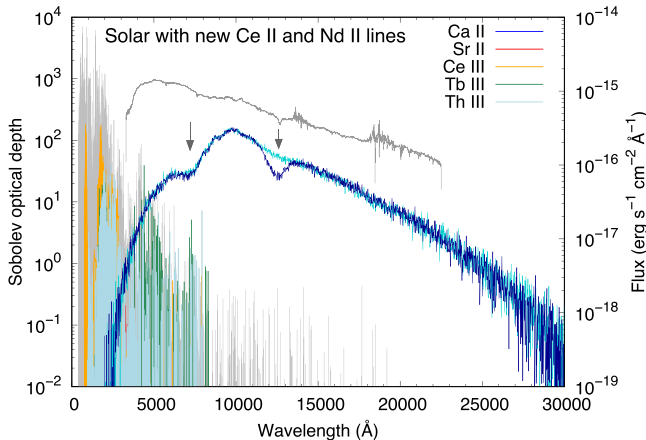

Figure 12. Same as the middle panel of Figure 7 (the S model), but with the additional transitions for Ce II (Cunha et al. 2017) and Nd II (Hasselquist et al. 2016) in the NIR wavelengths. The light-blue spectrum is that without the additional lines.

reason, the condition of X(Ca)/X(Sr) < 0.002 can be achieved only with the relatively high entropies of $s \geqslant 25\,k_{\mathrm{B}}$/nucleon (bottom panel), which inhibit nuclear equilibrium from being established. This implies that the blue component of AT2017gfo, which produces the Sr absorption line, comes from relatively high entropy ejecta. Such a condition may be realized in the viscously heated, post-merger ejecta (e.g., Just et al. 2015; Lippuner et al. 2017; Fujibayashi et al. 2020a) or in the shocked dynamical ejecta along the polar direction (e.g., Wanajo et al. 2014; Sekiguchi et al. 2015; Radice et al. 2018).

It should be noted that the conditions discussed above ($v \sim 0.2\,c$ and $s \geqslant 25\,k_{\mathrm{B}}$/nucleon) differ from the velocity and entropy distributions for our L model (the top panels of Figure 14 in Appendix B). However, this does not substantially affect our results shown in Sections 3 and 4.1 except for the Ca features. As cautioned in Wanajo (2018), our model obtained

by fitting a given reference abundance distribution is not necessarily the unique solution. We show the final abundances for the individual outflows with the fixed velocity of $\sim$0.2 c and the entropy of $\sim$10–25 k_{B}/nucleon in Figure 11. It is clear that a similar fit to that for the L model can be obtained with those parameters, except for the range around $Z = 20$–40. The distributions of Y_{e} for those entropies are similar to those for the L model, which tend to, however, be slightly shifted to the higher-Y_{e} side for a higher entropy.

Note also that we assume a solar r-process-like abundance distribution over a given range of atomic mass numbers to obtain our models (Section 2.1). If we relaxed this constraint, the ratio of X(Ca)/X(Sr) <0.002 would also be obtained with s $\sim$10 k_{B}/nucleon and $Y_{\mathrm{e}} \lesssim 0.35$ (Figure 10, bottom panel).

Our results imply that the Ca triplet line can be observed in future NS merger events. In particular, the post-merger ejecta with relatively high Y_{e} and relatively low entropy may have high ^{48}Ca abundance (Fujibayashi et al. 2020a). For such a case, we expect the Ca absorption feature with a moderate blueshift since the post-merger ejecta have relatively low expansion velocity ($v \sim 0.05\,c$). The detection of the Ca line in a future event will provide unique information on the ejecta condition as examined above for AT2017gfo.

Finally, it is interesting to note that ^{48}Ca is one of the isotopes whose origin remains a mystery. This isotope is synthesized most efficiently in the conditions of $Y_{\mathrm{e}} \sim 0.40$–0.42 and $\lesssim$15 k_{B}/nucleon (Meyer et al. 1996; Wanajo et al. 2013). Such a condition may be achieved in high-density Type Ia supernovae (Woosley 1997), electron-capture supernovae (Wanajo et al. 2013; Jones et al. 2019), low-mass core-collapse supernovae (Wanajo et al. 2018), collapsars (Fujibayashi et al. 2020b), or NS mergers (Wanajo 2018; Fujibayashi et al. 2020a). If the absorption line caused by the Ca II triplet appears in future kilonova spectra, we will be able to confirm the production of ^{48}Ca by NS mergers.

4.3. Importance of the NIR Line List

The spectra of AT2017gfo show absorption features in the NIR region (e.g., Pian et al. 2017). We have performed systematic calculations and radiative transfer simulations including the NIR lines, but it is difficult to unambiguously identify the absorption features. This is because the transition data are not sufficient in the NIR wavelengths compared with those in the UV to optical wavelengths. Atomic data for the NIR transitions have been limited mainly owing to a lack of high-resolution stellar spectroscopic observations and laboratory experiments in the NIR wavelengths.

Recently, new measurements have become available owing to the development of NIR spectroscopy such as the APOGEE survey (Allende Prieto et al. 2008). When the abundances in certain Galactic stars have been obtained from their optical spectra, one can estimate the transition probabilities for NIR lines by measuring these stars in the NIR wavelengths. In fact, two such analyses about Ce II ($Z = 58$) and Nd II ($Z = 60$) have been performed for the APOGEE survey, which give the transition probabilities for the 9 lines of Ce II (Cunha et al. 2017) and 10 lines of Nd II (Hasselquist et al. 2016) in H band.

We perform here the same simulations as in Section 3, but including these new lines. The synthetic spectrum for the S model with the new Ce II and Nd II lines is shown in Figure 12. The result shows an additional absorption feature at $\lambda \sim 13000$ Å, which is caused by the new Ce II lines. These
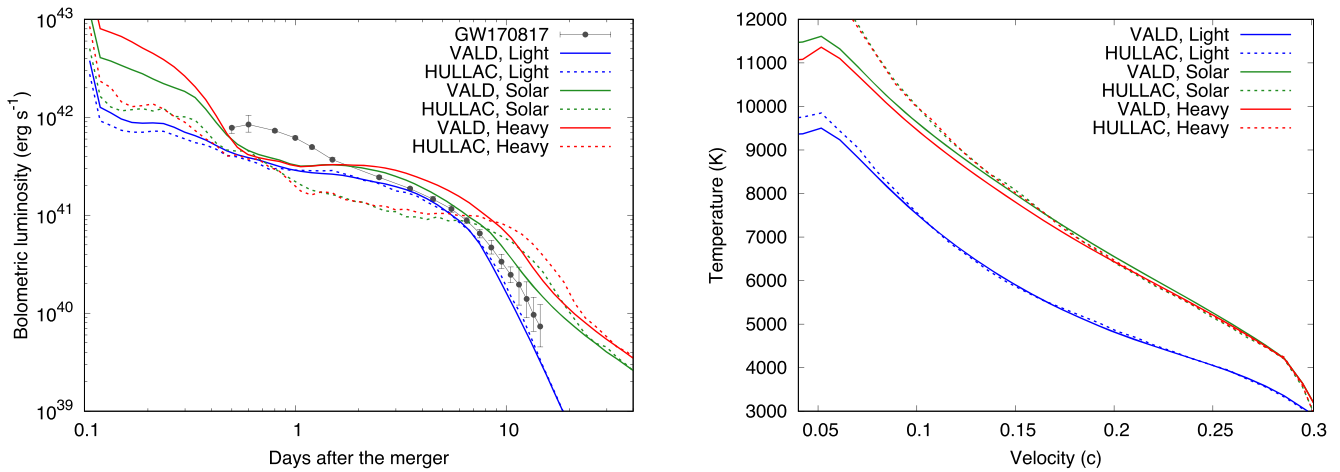
Figure 13. Left: bolometric light curves calculated with the two line lists. The bolometric light curve of GW170817 (the circles with error bars connected by lines; Waxman et al. 2018) is also shown for comparison. Right: radial distribution of temperature at $t = 1.5$ days. In both panels, the solid and dashed lines show the results with the line lists from the VALD database (Piskunov et al. 1995; Kupka et al. 1999; Ryabchikova et al. 2015) and HULLAC calculations (Tanaka et al. 2020), respectively. Different colors represent different models as shown in the legend.

Ce II lines are strong at around $T \sim 4000$–5000 K, similar to the Sr II lines. The H model also shows the same absorption feature, while the L model does not show it because of a small fraction of lanthanides (Table 1). Due to incompleteness of the line list in the NIR wavelengths, there is always a possibility that other unknown lines show stronger absorption lines. Therefore, it is not evident whether the Ce II lines can be observed in future (S- or H-model-like) events. Our analysis, however, demonstrates that atomic data in the NIR wavelengths are important to fully decode kilonova spectra, in particular at the later phase when kilonovae are brighter in NIR.

5. Conclusions

We have performed the systematic calculations of line strength for bound–bound transitions and radiative transfer simulations toward element identification in kilonova spectra. We have found that Sr II triplet lines appear in the spectrum at $v = 0.2\,c$ for our lanthanide-poor (L) model, which is consistent with the feature at $\lambda \sim 8000$ Å in the spectrum of GW170817/AT2017gfo. We have also found that Ca II triplet lines can appear in kilonova spectra. This is due to the fact that these two elements are coproduced in relatively high Y_e ejecta and their ions have similar atomic structures: only one electron in the outermost shell and the high transition probabilities for bound–bound transitions. We have shown that line strength strongly depends on the abundance distribution and temperature in the ejecta. For our lanthanide-rich (S or H) model, the spectra show the features of doubly ionized heavier elements, such as Ce, Tb, and Th. This points to the possibility that we can obtain the evidence of production of such heavy r-process elements in future NS merger events.

Since our results for the lanthanide-poor (L) model account for the presence of Sr II lines in the spectrum of GW170817/AT2017gfo, the line-forming region in the ejecta of GW170817 was likely dominated by relatively high Y_e (>0.30) material. Furthermore, we can constrain the physical condition of the ejecta by using the strength of Ca II and Sr II lines. Absence of the Ca II absorption in the spectra of GW170817/AT2017gfo implies that the X(Ca)/X(Sr) ratio should be less than 0.002. This ratio can be achieved in the NS merger ejecta with relatively high entropy ($s \gtrsim 25\ k_B$/nucleon)

for the velocity of $\sim 0.2\,c$, which may be realized in the post-merger ejecta or in the shock-heated dynamical ejecta. Since a high mass fraction of Ca (dominated by ^{48}Ca) is expected only with $Y_e \gtrsim 0.40$, the Ca II triplet can be used as a tracer of high-Y_e ejecta. We speculate that mildly Doppler-shifted Ca II lines from the high-Y_e post-merger ejecta with relatively small velocity will be identified in future events.

It is still challenging to identify the NIR absorption features in kilonova spectra because the atomic data are still incomplete in the NIR wavelengths. We have shown that the newly measured transitions of Ce II lines from the APOGEE survey affect the synthetic spectra in the NIR wavelengths. Although we cannot conclude that these lines will be certainly visible in future events, our study demonstrates the importance of updating the NIR line list to fully decode the spectra of kilonovae.

Appendix A
Effects of the Line List on the Light Curve

We inspect the impact of the adopted line list on the ejecta properties. The line list from the VALD database is not necessarily complete, in particular, for heavy elements in the NIR wavelengths. Thus, this incompleteness may affect the physical conditions of the ejecta such as temperature. Here we perform radiative transfer simulations as described in Section 3 with the theoretical line list from Tanaka et al. (2020). This line list was constructed by systematic atomic calculations using the HULLAC code. Transition data of this line list are not necessarily accurate in the relevant wavelengths, and thus they are not suitable for the identification of lines in kilonovae. However, since the data coverage is complete, it may give a more reliable estimate of the total opacity in the ejecta.

We confirm that the incompleteness of the VALD data does not have a significant impact on the temperature structure of the ejecta. The left panel of Figure 13 shows the results of light
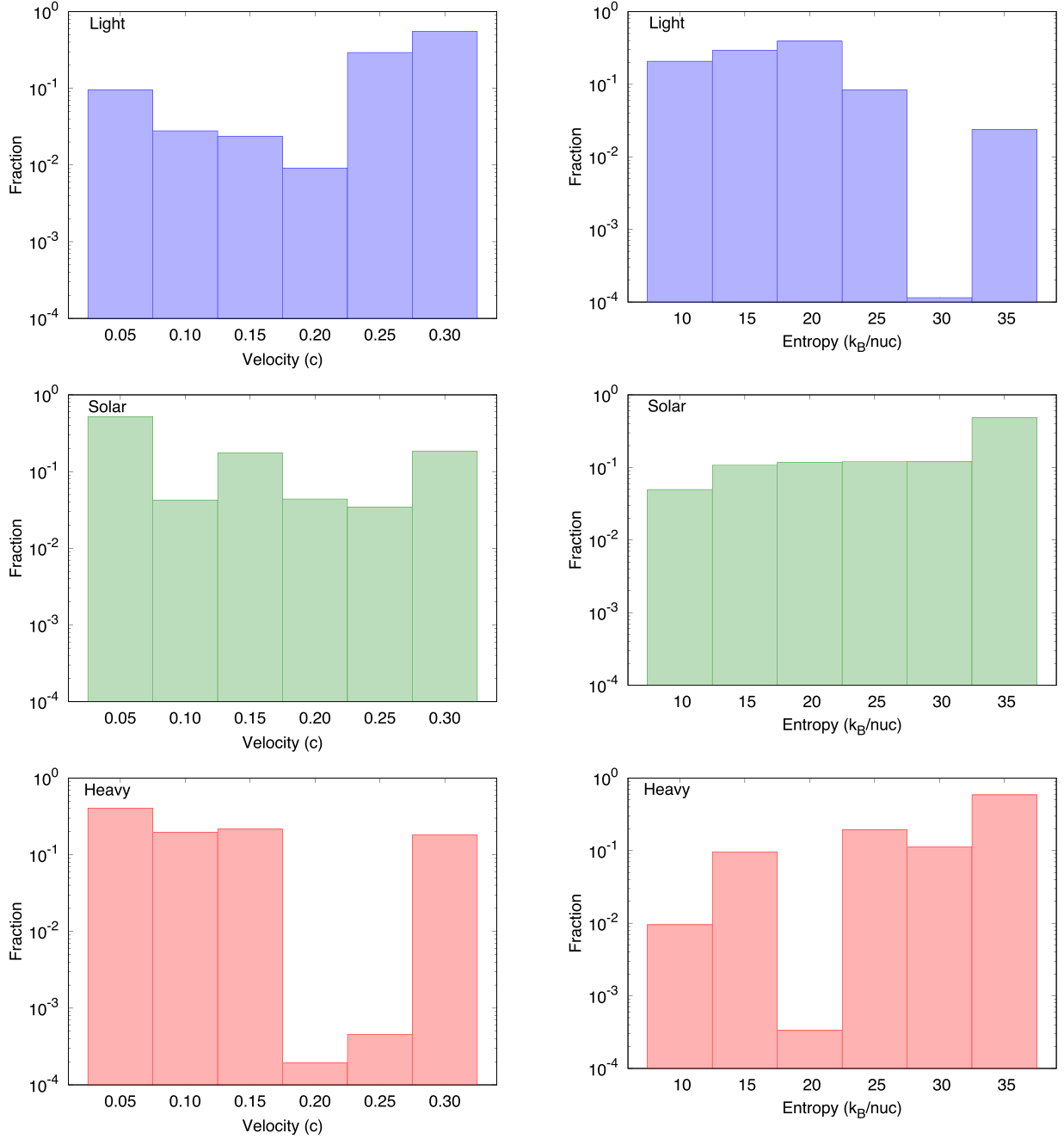
Figure 14. Histograms of velocity (left) and entropy (right) for L (top), S (middle), and H (bottom) models.

curves using both line lists. For the L model, which has a small fraction of lanthanides, the light curves are almost the same for both line lists. The light curves of the S and H models, which include a larger fraction of lanthanides, are more affected by the incompleteness of the line list: when the VALD database is used, our model underestimates the opacity, and thus the luminosity tends to be higher. Nevertheless, the temperature structure of the ejecta at $t = 1.5$ days after the merger is almost similar for all the models (right panel of Figure 13). This is because the temperature in the ejecta is mainly controlled by the heating rate, while the luminosity largely depends on the opacity (i.e., the line list). Because of the similarity of the temperature structure, we conclude that the incompleteness of the line list does not substantially affect our synthetic spectra at $t = 1.5$ days.

Appendix B
Properties of Models

We present the distributions of velocity and entropy for our L, S, and H models in Figure 14. These distributions are not necessarily the unique solutions for these models as noted in Section 4.2.

ORCID iDs

Nanae Domoto ⓘ https://orcid.org/0000-0002-7415-7954
Masaomi Tanaka ⓘ https://orcid.org/0000-0001-8253-6850
Shinya Wanajo ⓘ https://orcid.org/0000-0002-4759-7794
Kyohei Kawaguchi ⓘ https://orcid.org/0000-0003-4443-6984

References

Abbott, B. P., Abbott, R., Abbott, T. D., et al. 2017a, ApJL, 848, L12
Abbott, B. P., Abbott, R., Abbott, T. D., et al. 2017b, PhRvL, 119, 161101
Allende Prieto, C., Majewski, S. R., Schiavon, R., et al. 2008, AN, 329, 1018
Arcavi, I., Hosseinzadeh, G., Howell, D. A., et al. 2017, Natur, 551, 64
Banerjee, S., Tanaka, M., Kawaguchi, K., Kato, D., & Gaigalas, G. 2020, ApJ, 901, 29
Barnes, J., & Kasen, D. 2013, ApJ, 775, 18
Barnes, J., Kasen, D., Wu, M.-R., & Martínez-Pinedo, G. 2016, ApJ, 829, 110
Biémont, E., Palmeri, P., & Quinet, P. 1999, Ap&SS, 269, 635
Biémont, E., Palmeri, P., Quinet, P., Zhang, Z. G., & Svanberg, S. 2002a, ApJ, 567, 1276
Biémont, E., Quinet, P., & Ryabchikova, T. A. 2002b, MNRAS, 336, 1155
Coulter, D. A., Foley, R. J., Kilpatrick, C. D., et al. 2017, Sci, 358, 1556
Cowan, J. J., Sneden, C., Beers, T. C., et al. 2005, ApJ, 627, 238
Cowan, J. J., Sneden, C., Lawler, J. E., et al. 2021, RvMP, 93, 015002
Cunha, K., Smith, V. V., Hasselquist, S., et al. 2017, ApJ, 844, 145
Eastman, R. G., & Pinto, P. A. 1993, ApJ, 412, 731
Eichler, D., Livio, M., Piran, T., & Schramm, D. N. 1989, Natur, 340, 126
Evans, P. A., Cenko, S. B., Kennea, J. A., et al. 2017, Sci, 358, 1565
Fernández, R., & Metzger, B. D. 2013, MNRAS, 435, 502
Fontes, C. J., Fryer, C. L., Hungerford, A. L., Wollaeger, R. T., & Korobkin, O. 2020, MNRAS, 493, 4143
Freiburghaus, C., Rosswog, S., & Thielemann, F. K. 1999, ApJL, 525, L121
Fujibayashi, S., Kiuchi, K., Nishimura, N., Sekiguchi, Y., & Shibata, M. 2018, ApJ, 860, 64
Fujibayashi, S., Shibata, M., Wanajo, S., et al. 2020a, PhRvD, 101, 083029
Fujibayashi, S., Shibata, M., Wanajo, S., et al. 2020b, PhRvD, 102, 123014
Fujibayashi, S., Wanajo, S., Kiuchi, K., et al. 2020c, ApJ, 901, 122
Goriely, S., Bauswein, A., & Janka, H.-T. 2011, ApJL, 738, L32
Hasselquist, S., Shetrone, M., Cunha, K., et al. 2016, ApJ, 833, 81
Honda, S., Aoki, W., Ishimaru, Y., Wanajo, S., & Ryan, S. G. 2006, ApJ, 643, 1180
Hotokezaka, K., Kiuchi, K., Kyutoku, K., et al. 2013, PhRvD, 87, 024001
Jones, S., Côté, B., Röpke, F. K., & Wanajo, S. 2019, ApJ, 882, 170
Just, O., Bauswein, A., Ardevol Pulpillo, R., Goriely, S., & Janka, H. T. 2015, MNRAS, 448, 541
Karp, A. H., Lasher, G., Chan, K. L., & Salpeter, E. E. 1977, ApJ, 214, 161
Kasen, D., Badnell, N. R., & Barnes, J. 2013, ApJ, 774, 25
Kasen, D., Fernández, R., & Metzger, B. D. 2015, MNRAS, 450, 1777
Kasen, D., Metzger, B., Barnes, J., Quataert, E., & Ramirez-Ruiz, E. 2017, Natur, 551, 80
Kawaguchi, K., Shibata, M., & Tanaka, M. 2018, ApJL, 865, L21
Korobkin, O., Rosswog, S., Arcones, A., & Winteler, C. 2012, MNRAS, 426, 1940
Kramida, A., Ralchenko, Y., Reader, J. & NIST ASD Team 2019, NIST Atomic Spectra Database (ver. 5.7.1) (Gaithersburg, MD: National Institute of Standards and Technology) https://physics.nist.gov/asd
Kupka, F., Piskunov, N., Ryabchikova, T. A., Stempels, H. C., & Weiss, W. W. 1999, A&AS, 138, 119

Kurucz, R. L. 2017, Robert L. Kurucz on-line Database of Observed and Predicted Atomic Transitions https://www.astro.uu.se/valdwiki/linelistRefs
Lattimer, J. M., & Schramm, D. N. 1974, ApJL, 192, L145
Li, L.-X., & Paczyński, B. 1998, ApJL, 507, L59
Lippuner, J., Fernández, R., Roberts, L. F., et al. 2017, MNRAS, 472, 904
Metzger, B. D., & Fernández, R. 2014, MNRAS, 441, 3444
Metzger, B. D., Martínez-Pinedo, G., Darbha, S., et al. 2010, MNRAS, 406, 2650
Meyer, B. S., Krishnan, T. D., & Clayton, D. D. 1996, ApJ, 462, 825
Perego, A., Radice, D., & Bernuzzi, S. 2017, ApJL, 850, L37
Perego, A., Rosswog, S., Cabezón, R. M., et al. 2014, MNRAS, 443, 3134
Perego, A., Vescovi, D., Fiore, A., et al. 2020, arXiv:2009.08988
Pian, E., D'Avanzo, P., Benetti, S., et al. 2017, Natur, 551, 67
Piskunov, N. E., Kupka, F., Ryabchikova, T. A., Weiss, W. W., & Jeffery, C. S. 1995, A&AS, 112, 525
Prantzos, N., Abia, C., Cristallo, S., Limongi, M., & Chieffi, A. 2020, MNRAS, 491, 1832
Radice, D., Perego, A., Hotokezaka, K., et al. 2018, ApJ, 869, 130
Roberts, L. F., Kasen, D., Lee, W. H., & Ramirez-Ruiz, E. 2011, ApJL, 736, L21
Roederer, I. U., Lawler, J. E., Sobeck, J. S., et al. 2012, ApJS, 203, 27
Rosswog, S., Liebendörfer, M., Thielemann, F. K., et al. 1999, A&A, 341, 499
Rosswog, S., Sollerman, J., Feindt, U., et al. 2018, A&A, 615, A132
Ruffert, M., Janka, H. T., Takahashi, K., & Schaefer, G. 1997, A&A, 319, 122
Ryabchikova, T., Piskunov, N., Kurucz, R. L., et al. 2015, PhyS, 90, 054005
Ryabchikova, T., Ryabtsev, A., Kochukhov, O., & Bagnulo, S. 2006, A&A, 456, 329
Ryabchikova, T., Sachkov, M., Weiss, W. W., et al. 2007, A&A, 462, 1103
Sekiguchi, Y., Kiuchi, K., Kyotoku, K., & Shibata, M. 2015, PhRvD, 91, 064059
Shibata, M., Fujibayashi, S., Hotokezaka, K., et al. 2017, PhRvD, 96, 123012
Siqueira Mello, C., Spite, M., Barbuy, B., et al. 2013, A&A, 550, A122
Smartt, S. J., Chen, T. W., Jerkstrand, A., et al. 2017, Natur, 551, 75
Sobolev, V. V. 1957, SvA, 1, 678
Tanaka, M., & Hotokezaka, K. 2013, ApJ, 775, 113
Tanaka, M., Hotokezaka, K., Kyutoku, K., et al. 2014, ApJ, 780, 31
Tanaka, M., Kato, D., Gaigalas, G., et al. 2018, ApJ, 852, 109
Tanaka, M., Kato, D., Gaigalas, G., & Kawaguchi, K. 2020, MNRAS, 496, 1369
Tanaka, M., Utsumi, Y., Mazzali, P. A., et al. 2017, PASJ, 69, 102
Theodosiou, C. E. 1989, PhRvA, 39, 4880
Utsumi, Y., Tanaka, M., Tominaga, N., et al. 2017, PASJ, 69, 101
Valenti, S., Sand, D. J., Yang, S., et al. 2017, ApJL, 848, L24
Wanajo, S. 2018, ApJ, 868, 65
Wanajo, S., Janka, H.-T., & Müller, B. 2013, ApJL, 767, L26
Wanajo, S., Müller, B., Janka, H.-T., & Heger, A. 2018, ApJ, 852, 40
Wanajo, S., Sekiguchi, Y., Nishimura, N., et al. 2014, ApJL, 789, L39
Watson, D., Hansen, C. J., Selsing, J., et al. 2019, Natur, 574, 497
Waxman, E., Ofek, E. O., Kushnir, D., & Gal-Yam, A. 2018, MNRAS, 481, 3423
Woosley, S. E. 1997, ApJ, 476, 801